

Investigation of the Mechanical Behaviour of Porous Silicon Neural Microprobes

Rayan Fayad, Soumaya Berro, Bakri AbdulHay, Hussein Hajj-Hassan, Hassan M. Khachfe, Mohamad Hajj-Hassan

Dept. of Biomedical Engineering

Lebanese International University

Beirut, Lebanon

rayanfayad@gmail.com, Soumaya.berro@liu.edu.lb, bakri.abdulhay@liu.edu.lb, hussein.hajjhassan@liu.edu.lb, hassan.khachfe@liu.edu.lb, mohamad.hajjhassan@liu.edu.lb

Abstract—Porous silicon has become the gold standard when it comes to improving biocompatibility and bioactivity. For this reason, it has become a primary candidate in neural electrodes research and development. Consequently, the purpose of this work was to investigate the mechanical strength of porous silicon neural electrodes. Thus, a finite element model representing the proposed electrode was generated. Mechanical simulation was done on porous and non-porous electrodes using COMSOL® Multiphysics. Results showed that porosity decreased the mechanical strength of the neural electrode without risking the mechanical requirements for neural applications.

Keywords- *biocompatibility; finite element model; failure analysis; neural microelectrodes; porous silicon.*

I. INTRODUCTION

The application of technological advances to cure neurological diseases has long seized the attention of researchers in neural engineering. The first acknowledged use of electrical current in an approach to treat a neural disease goes back to the year 1757. This has gravely evolved nowadays due to progresses in neuroscience and microtechnology, where a wide range of neural electrodes have been fabricated and used in neuroscience and neural prosthetic research (brain machine interfaces) [1], [2], [3], [4].

Neural electrodes, which are micro structures that are implanted in the brain, serve as a communication channel between the electro-active neurons in the brain and an outer electronic circuitry [5], [6], [7].

These electrodes are used in both recording action potentials from neurons and stimulating specific brain regions. The electrical stimulation of nerve tissue and recording of neural electrical activity are the foundation of evolving prostheses and treatments for spinal cord injury, stroke, sensory deficits, and neurological disorders such as seizures, epilepsy, and migraine [7], [8].

As schematized in Figure 1, brain-computer interfaces (BCIs), which incorporate the use of neural electrodes, provide a linkage between the brain and the external world by computer processing the recorded neural signal to extract the subject's command to control an external device. This technology can allow restoring neural functions of patients with severe neurologic impairment [9].

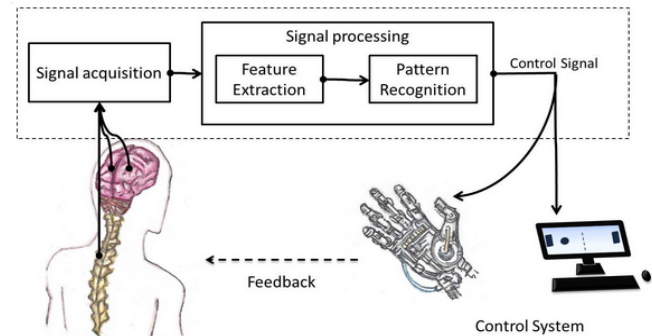


Figure 1. Basic components of a Brain-Computer Interface [10].

When it comes to the general characteristics of a neural electrode, it is notable to mention that the ideal electrode should have a very small cross section in a way that it displaces or damages as little tissue as possible during insertion in order to minimize neural damage. Another reason that makes the small footprint of the neural electrode desirable is that the smaller size allows the selective targeting of the desired neurons, thus improving the signal-to-noise ratio of the recorded activity or targeting a very specific region to be stimulated. On the other hand, the ideal electrode should also be wide enough to incorporate a large number of electrode sites to be able to record and reliably separate different neurons. Regardless of the size, the electrode must be optimized for long term biocompatibility and should have enough mechanical strength to survive the various forces to which it is subjected during insertion and retraction forces while implantation [11], [12]. Several types of neural electrodes have been designed and developed until this day (Figure 2). In the 1950s, the initial use of implantable microelectrodes to record electrical activities in the extracellular environments was traced [13], [14], [15]. These microelectrodes, also known as microwires (Figure 2-A), have the longest history and the widest use in the field. Microwires are wires made of a conducting metal, such as platinum, gold [16], tungsten [17], iridium [18], or stainless steel [19]. Each microelectrode is composed of a metal wire entirely insulated except for its tip; it is left exposed acting as a recording site [20], [21], [22]. Later, the use of microelectrodes advanced into offering the ability of provide multiple metal electrode arrays [23].

Those were constructed by pasting individual microelectrodes together [24], [25], or by gathering several metal wires on a ceramic plate [26]. However, the drawback of this type is that only one recording site is available, which is located at the exposed tip. Hence, any attempt to increase the number of recording sites would include increasing the number of electrodes. This will in turn increase the total size of the electrode, which is a feature that is not usually preferred due to the resulting neural tissue damage it might cause. Furthermore, though a metal microelectrode has the advantage of simplicity in terms of the process of fabrication, this simplicity is the reason of a major drawback, which is the lack of common standards and automation. Thus, the characteristics of the electrode would vary from one institution to another or from one laboratory to another [11].

This drawback was solved with the introduction of silicon based neural electrodes that emerged with the development of microfabrication techniques and the advancement in microelectronics and microelectrochemical systems (MEMS) [27], [28], [29]. It was in the 1970s when Wise and Angell have published a silicon-based electrode to interface neural tissues [30], [31]. Generally speaking, silicon electrodes offered a superiority over the metal microelectrodes since they allowed an increased number of recording sites without increasing the whole size of the electrode as well as their precise and reproducible fabrication [32]. In other words, by using the photolithography process, the designer would be able to gain control over the recording site size, shape and spacing enabling multiple recording sites to be placed at variable heights on a single electrode shank. Consequently, it would be possible to introduce an increased number of recording sites in a small volume, which is not possible with metal electrode arrays [28]. In addition, silicon offers well-recognized biocompatibility and mechanical properties appropriate for neural electrodes [11]. Well-known examples of silicon neural electrodes are the Utah [33], [34] and the Michigan [6], [35], [36], [37] electrodes. The Utah electrode array (Figure 2-C to the left) is a famous MEMS microelectrode array, which is a widely used type of implantable interface in BCI. The fabrication of the Utah electrode array includes micromachining monocrystalline silicon blocks to form a shape similar to a bed of nails. As for the Michigan electrode (Figure 2-C to the right), it is composed of a boron-diffused silicon substrate, a silicon dioxide and silicon nitride dielectric stack, polysilicon traces, and iridium electrode sites [38].

Another type of electrodes is the polymer-based neural electrode characterized by improved flexibility and biocompatibility as well as the advantage of a simpler fabrication process [39], [40], [41], [42], [43]. Traditionally, in the process of fabrication of a neural silicon electrode, the electrode was usually insulated by a silicon nitride or silicon dioxide layer. This was swapped by the use of polymeric materials in neural electrodes [44], [45], [46]. Serving the purpose of forming a biocompatible

interface between the neural electrode and the brain tissue where it is implanted, several biocompatible polymers have been used. These include the use of polyimide and Parylene-C, which play the role of insulating the metal and silicon region of the electrode [46], [47], [48]. However, a significant limitation of this type of electrodes is that they are not stiff enough to penetrate the brain tissue on their own. In other words, these electrodes suffer from lack of rigidity, which leads to less accurate neural targeting due to the buckling of the electrode during the insertion phase [11].

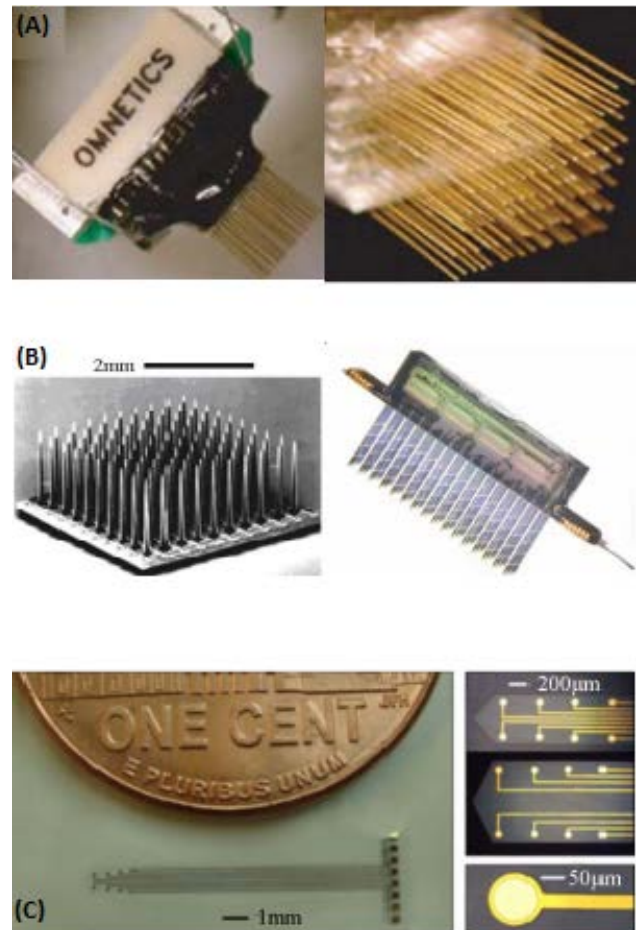


Figure 2. Types of neural electrodes [15].

This article covers the simulation of the mechanical behavior of porous silicon neural electrode. The next section presents the major limitation of present types of chronically implanted neural electrodes due to the resultant brain tissue response. Section III shows how using porous silicon plays a critical role in solving these limitations. Section IV introduces the design of the proposed electrode. Section V discusses the simulation strategy followed. Section VI details the results yielded.

II. LIMITATION OF CHRONICALLY IMPLANTED NEURAL ELECTRODES: THE BRAIN TISSUE RESPONSE

While the previously mentioned systems function well during acute recordings, they frequently do not succeed to operate reliably in clinically relevant chronic settings. The reason why these electrodes fail has been attributed to the brain tissue reaction against these implants. This brain tissue response is provoked by the neural injury upon the implantation of the electrode. Consequently, the resultant tissue response threatens the long-term functioning of the neural electrode. This response includes two major stages known as the acute immune and the chronic immune responses [20], [49], [50], [51] as illustrated in Figure 3.

The implantation of any neural electrode is always a traumatic procedure. When a neural electrode is inserted into the brain, it breaches the vasculature, the extracellular matrix, and destroys neuronal and glial processes in its path. This gives rise to the acute immune response. Forthwith, by displacing structures along its way, the electrode would cause an alternation in the pressure status in that region inducing a high-pressure region around the electrode. These factors combined cause edema and hemorrhage near the implant. Accordingly, the wound healing process will be commenced as a result. Since the blood vessels are disrupted, this provokes them to discharge erythrocytes, activates platelets, clotting factors, and the complement cascade. This process will assist in macrophage stimulation and the beginning of tissue reconstruction. One day after implementation, activated microglia will show up around the implant.

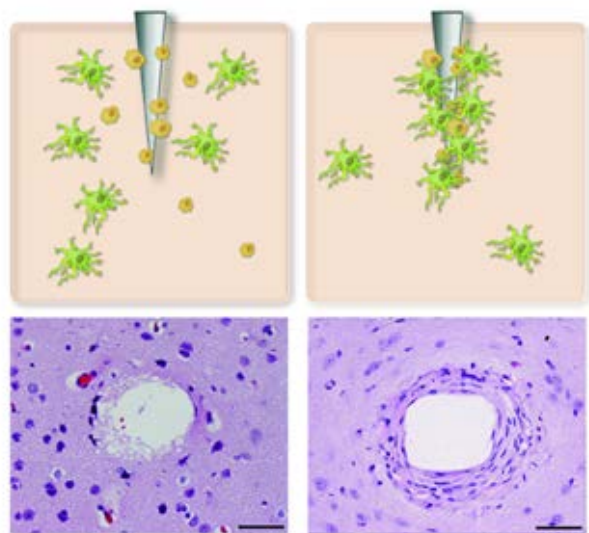


Figure 3. Acute and chronic neural injury caused by the insertion of the neural electrode into the brain cortex [49].

Soon enough, the acute immune response will start to deteriorate, which is directly followed by a chronic immune response. The most influential participants in this phase are reactive astrocytes and activated microglia [52],

[53]. This response results in the formation of an encapsulation layer termed the “glial scar” around the electrode. Activated microglia will be engaged in the phagocytosis of the foreign matter for eventual degradation. However, the most significant event that is notable in the long-term response to the chronically implanted electrode is the formation of the encapsulation layer. This glial scar is a reactive glial tissue with reactive astrocytes being its major element. It isolates the implanted neural electrode from the surrounding tissue in a process that resembles fibrotic encapsulation reaction encountered with non-degradable implants in soft tissues. This encourages the inhibition of diffusion and increases the impedance of the tissue-electrode interface. In addition, this also extends the distance between the electrode and the nearest desired neurons. Accordingly, the neurite extensions will find themselves in a non-encouraging environment for growth, the thing that pushes redeveloping neural processes away from the recording sites. This leads to signal deterioration [20], [51], [54], [55], [56].

III. ADVANTAGES OF POROUS SILICON FOR NEURAL ELECTRODES

As stated earlier, interactions between the brain tissue and the electrode are critical in determining the functional performance of the electrode. Various strategies have been investigated and experimented as an attempt to minimize the immune response towards the chronically implanted neural electrode. Some related the degree of the immune response to the size of the electrode [56]. Others thought that the severity of the immune response can be controlled by altering the shape of the electrode [57]. Additionally, it has been proven that tissue response is highly dependent on the surface topography [58]. In the latter approach, it has been tested and proved that rough surfaces are more biocompatible than smooth surfaces [59]. An alternation in the surface topography so that it would be transformed from smooth to rough could be by making the surface porous. In particular, the use of porous silicon as the material that the implants would be made of has shown enhanced biocompatibility and bioactivity [60], [61], [62].

For instance, in a study performed by Hajj-Hassan et al. [62], the biocompatibility and bioactivity of porous silicon wafers (Si) was assessed by examining the survival and replication of mesenchymal stromal cells (MSC) isolated from the bone marrow of wild type mice. These results were compared with that of cells growing in 2D culture on tissue culture plastic (TCP) and on smooth titanium (SmTi), which is well known for its superiority (gold standard) for the manufacture of implants. In the first experiment performed, bone marrow derived MSC were seeded in porous silicon wafers etched to a depth of 20 μm (Si20) in 12 well plates and harvested after 3, 6, and 9 days of culture. Control cells plated at the same

density on tissue culture plastic were harvested at 6 days and stained with toluidine blue to visualize the cells. Results showed that the Si20 substrate supported the MSC growth. Additionally, an Alamar Blue metabolic assay was used to analyze the metabolic activity of cells grown porous silicon substrates etched to a depth of 20 μm (Si20) or 30 μm (Si30) and compared with TCP or smooth titanium, which is a common implant material. Representative results of the Alamar Blue assay, shown in Figure 4(A), indicate a small increase in metabolic activity of the cells grown on Si20 and Si30 samples compared to smooth titanium and tissue culture plastic controls. The cell counts indicated a steady increase in numbers that appeared to be dependent on the substrate on which they were grown.

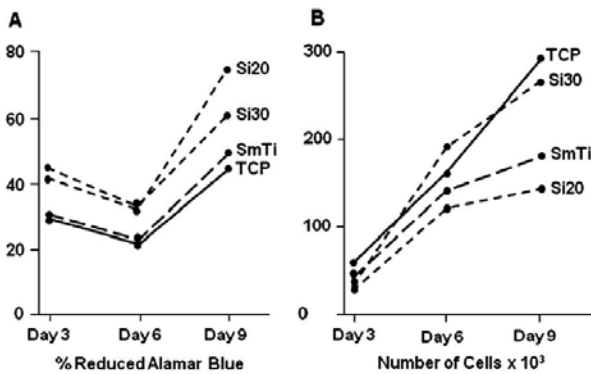


Figure 4. Quantitative analysis of MSC grown on porous silicon etched to a depth of 20 μm (Si20), 30 μm (Si30), commercial grade smooth titanium (SmTi) and tissue culture plastic (TCP) using the Alamar Blue assay to assess the metabolic activity [61].

So, it has been shown that the introduction of the pores improves the biocompatibility and bioactivity. However, a fundamental question imposes itself regarding whether their introduction influences the mechanical strength of the electrode. In other words, we are interested in knowing if the implanted porous electrode will still survive the forces exerted by the brain environment during and after implantation. The solution to this question is demonstrated in the sections that follow.

IV. DESIGN

The following section covers the design of the proposed neural electrode. The developed neural electrode is constructed using a silicon substrate (Young's Modulus = 190 GPa & Poisson's ratio = 0.17) and is considered to be ultra-long with a total length of 10.5 mm. Its overall structure is tapered, which facilitates the penetration. The geometry of the electrode is sectioned into three main regions; a base region, a measuring region incorporating the metal recording sites, and a piercing region. The base region measures 250 μm in length with a width of 350 μm at the base that rapidly reduces to a width of 150 μm . This design aids in diminishing brain tissue damage and displacement. The measuring region that has a length of 10

mm starts with a width of 150 μm at the base and ends up with 50 μm at the other end. Following the measuring region is the piercing region, which has a length of 250 μm and is designed to be of 10 μm width at the end of the probe.

The relative dimensions of these regions are indicated in Figure 5. The electrode was implemented using COMSOL[®] Multiphysics 4.3 as depicted in Figure 6.

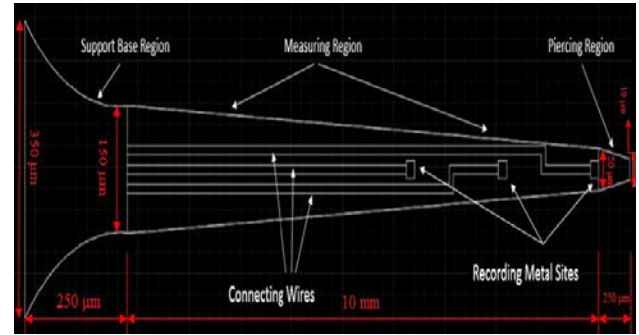


Figure 5. 2D drawing of the designed electrode with annotations.

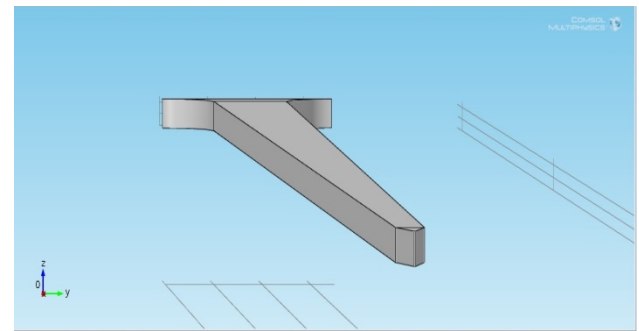


Figure 6. Complete 3D model of electrode.

In the selection of the criteria to develop the pores, we chose the various dimensions of the pores according to the limitations imposed by the standard fabrication processes followed. In other words, our selection should be similar to what is available and applicable in the fabrication world. The medium in which the probe is to be inserted contains features that exhibit micro and nano dimensions. In an attempt to mimic this medium, we select the radius of the pores in the low micro-level and the pore depth was constant at 0.6 μm due to fabrication standards. Our approach included pores with a cylindrical geometry with a radius of 1.5 μm (Figure 7).

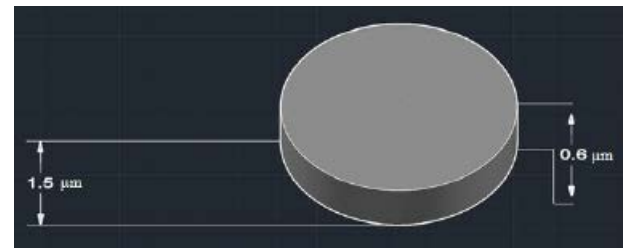


Figure 7. 3D pore geometry with annotated dimensions.

The distance separating the pores in both the x and y directions is approximately 3 μm . As mentioned earlier, each pore had a depth of 0.6 μm . The pores distributed along the entire geometry of the probe except at the regions where the metal sites and connecting wires are placed. This is depicted in Figures 8 and 9, respectively.

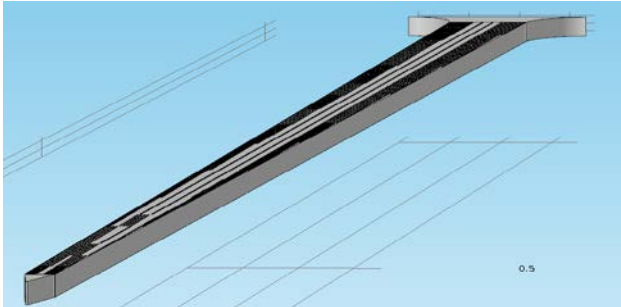


Figure 8. 3D model of porous electrode in COMSOL[®] Multiphysics.

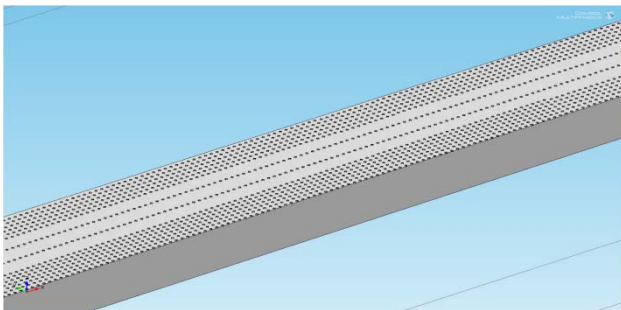


Figure 9. A close up of the arrays of pores.

V. SIMULATION STRATEGY

As an attempt to predict the mechanical behavior of the proposed probe, both a finite element model simulation approach and an analytical calculation approach were performed for both a non-porous and porous electrode. This is targeted to approximate the differences between the two approaches.

The aim is to mimic the forces applied to the electrode during and after insertion into the brain. The naturally imposed forces can be classified into three different cases; case one includes the application of two axial forces, which are imposed during the penetration phase, case two includes the application of a single axial force, which occurs directly after penetration and may cause the buckling of the probe, and case three includes the application of a vertical force, which occurs after the probe implementation and may result in the bending of the probe. Out of plane forces rarely happen because when the probe is implanted it is mounted on a motion controller, which goes in one direction towards the brain (x-axis). Hence, the force along x-axis will be focused upon throughout this paper in the different strategies followed.

Most importantly, in both strategies, the maximum critical stress was to be yielded and this stress was to be

compared to the yielding stress of the material. The yielding stress of Silicon is approximately equal to 1GPa [63]. It is essential to mention that the maximum critical stress in both strategies followed is determined using the “Maximum Distortion Energy Theory”, also known as the “R. von Mises Theory”, which is demonstrated in equation (1) below [64], where σ_e is the effective stress or von Mises stress and $\sigma_{1,2}$ are the principal stresses.

$$\sigma_e = (\sigma_1^2 + \sigma_1\sigma_2 + \sigma_2^2)^{1/2} \quad (1)$$

The maximum distortion energy theory is one of the famous failure theories for ductile material. This theory states that failure is predicted to occur in the multiaxial state of stress when the distortion energy per unit volume becomes equal to or exceeds the distortion energy per unit volume at the time of failure in a simple uniaxial stress test using a specimen of the same material [65]. In other words, a given structural material is safe as long as the maximum value of the distortion energy per unit volume in that material remains smaller than the maximum distortion energy per unit volume required for causing yield in a tensile test specified of the same material. The simulated effective stress is then compared to the yielding stress of the material.

Regarding the Finite Element Model (FEM) strategy increasing forces were gradually applied on both the porous and the non-porous electrodes until the yield stress of the material is reached. These forces were applied on the front face of the piercing tip while fixing the back face of the support base region as illustrated in Figure 10.

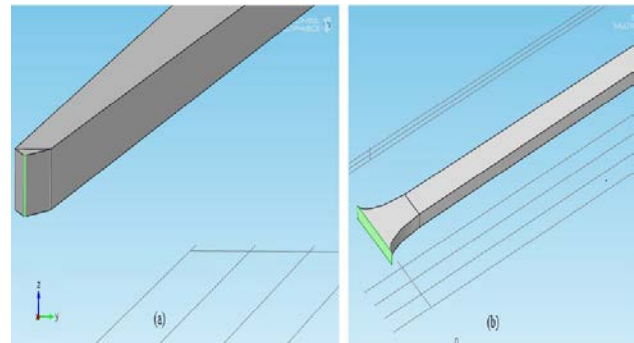


Figure 10. Marked in green is (a) Area on which the stress is applied, (b) area which is a fixed constraint.

It is notable to mention that during the simulation of the porous electrode, pores were restricted to the weakest regions of the electrode as seen in Figure 11.

This was done to reduce the computational complexity. These regions are the middle of the electrode (during axial loads), and the base region of the electrode (during vertical loads) [66].

As for the analytical strategy, the internal forces that generated in the porous and the non-porous probes upon the application of the different combination of loads in the

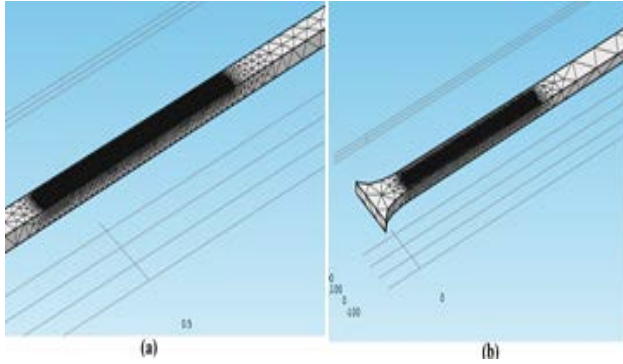


Figure 11. (a) Porous region on the middle of the probe, (b) porous region on the base.

three cases were calculated. These internal forces were used to calculate the resulting principal stresses according to equation (2) below, where σ_x and σ_y are the induced stresses and τ_{xy} is the induced shear stress.

$$\sigma_{1,2} = \frac{\sigma_x + \sigma_y}{2} \pm \sqrt{\left(\frac{\sigma_x - \sigma_y}{2}\right)^2 + \tau_{xy}^2} \quad (2)$$

These principal stresses were then employed either to calculate the maximum distortion energy or the von Mises stress in case 1 (x-axis and y-axis axial forces) and case three (z-axis vertical force) or to compare with the critical stress and the elastic stress in case 2 (x-axis axial force). The calculation of the von Mises stresses is done by the previously mentioned equation. Meanwhile, the calculation of the critical stress is done by the calculation of the critical buckling load, which is yielded by the extended Euler's Formula stated below [67].

$$P_{critical} = \frac{\pi^2 \times E \times I}{(KL)^2} \quad (3)$$

$$\sigma_{critical} = \frac{P_{critical}}{A} \quad (4)$$

where A is the cross-sectional area upon which the load is applied, $P_{critical}$ is the critical load, E is the Young's Modulus of the material, I is the moment of inertia of the cross-section, KL is the effective length of the electrode. In the case of a column fixed at its base K is equal to 2 [67].

Solving the equations will give us an idea about how far the finite element model is from the analytical equations. As mentioned earlier, out of plane forces rarely happen because when the probe is implanted it is mounted on a motion controller, which goes in one direction towards the brain (x-axis). Hence, the force along x-axis will be focused upon in the analytical strategy.

However, before starting with the FEM strategy, and in order to study the stability of the FEM with respect to the results obtained, we tried different element sizes until the results started converging to the same average values. As it will be shown in Table I in the results, the element size is changed, the probe is meshed, and the number of elements is measured.

VI. RESULTS

The following section elaborates on the results obtained from the study done to assess the stability of the FEM and the simulation of both the porous and non-porous electrodes in the FEM strategy and the analytical strategy. For each simulation, a plot of the induced principal stress in MPa versus the length of the electrode in μm as a result of applying the loads is obtained. Subsection 1 will cover the results yielded in from the FEM stability study, subsection 2 will demonstrate the results yielded from the analytical strategy, subsections 3, 4, and 5 will cover the results yielded from the FEM simulation strategy in the three different cases. Subsection 6 will show a comparison between the analytical and the FEM strategies.

1) Results of the FEM Stability Study

As mentioned earlier, different element sizes were chosen until the results starting converging to the same average values. As shown in Table I, the element size is changed, the probe is meshed, and the number of elements is measured.

TABLE I. ELEMENT SIZE VERSUS THE NUMBER OF ELEMENTS FOR THE MODELLED NEURAL PROBE

Element Size (μm)	Number of Elements
2000	265
1000	311
500	426
250	532
125	961
72	2041
36	13712
18	133688
9	1158561
4	13900199

The results obtained are also plotted in a curve as illustrated in Figure 12. One can notice the exponential increase in the number of elements when the element size decreased.

The results were also calculated for different element size. Element size was decreased until the finite element model started converging to a range of close values as shown in Table II.

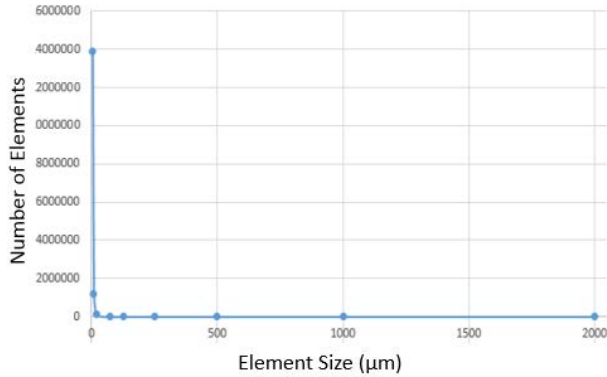


Figure 12. A plot showing the element size versus the number of elements.

The results obtained are plotted on a curve as shown in Figure 13. It is important to note that the y-axis starts from 1000 MPa. Starting from 0 MPa the result was a straight horizontal line, hence it was changed to start from 1000 MPa to shown the fluctuations before the results converged.

TABLE II. ELEMENT SIZE VERSUS VON-MISES STRESS

Element Size (µm)	Result (MPa- Von-Mises)
2000	1053.1
1000	1076.45
500	1066.91
250	1081.88
125	1077.49
72	1082.47
36	1064.15
18	1063.12
9	1064.29
4	1064.76

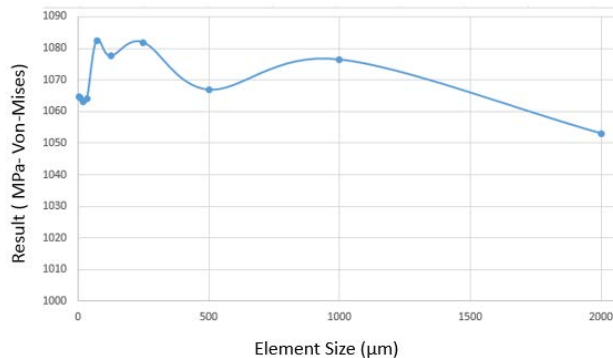


Figure 13. A plot showing the element size versus the number of elements.

2) Results of the Analytical Strategy

It is beneficial to reiterate that the results presented in this section are yielded by performing calculations upon the application of the axial force since is it the most significant.

For the non-porous electrode, upon the application of the maximum force of 527.5 mN the internal stress induced was found to be equal to 1055 MPa. Meanwhile, upon the application of the minimum force of 2.42 mN [68], the internal stress induced was found to be 4.94 MPa. Additionally, the critical force and critical stress that are required for comparison were also calculated according to the previously mentioned equations and were found to be equal to 4.4 mN and 8.8 MPa, respectively.

Regarding the porous electrode, two main parameters must be obtained in order to characterize the mechanical behavior analytically. The parameters are the young’s modulus of silicon at the specific porosity and the yield stress at which the material will fail at this porosity. The porosity was calculated by taking into consideration the number of pores and their cylindrical volume with respect to the total volume of the electrode. This is demonstrated in equations (5) and (6).

$$Ratio\ of\ Volume = \frac{V_{pores}}{V_{electrode}} = \frac{8.396 \times 10^{-14}}{5.35 \times 10^{-11}} = 1.56 \quad (5)$$

$$\% Porosity = \frac{Ratio\ of\ Volume \times 100}{100} = \frac{1.569 \times 10^{-3} \times 100}{100} \cong 0.16\% \quad (6)$$

In order to obtain the young’s modulus of porous silicon at our porosity, different studies were researched. These studies are illustrated in Figure 14. The closest study for the change in young’s modulus relative to the percentage of porosity is the one done by Al-Douri et al. [69]. As for the yield stress of our porous silicon material, there are no previous studies in the literature so far. Since the geometry of the porous electrode is the same as the non-porous one, and since both are of the same material we will do the following assumption. We will assume that both will have the same yield strain that will to failure. Having this yield strain and knowing the young’s modulus we are able to calculate the yield stress of our porous silicon according to Hook’s law given in the equation below.

$$\sigma = E \times \epsilon_y \quad (7)$$

Since in the selected literature the closest young’s modulus to ours, which is 190 GPa, is 185, we will redo the FEM simulation at 185 GPa in order to compare it to the analytical solution. After repeating the simulation for case 2 only at 185 GPa, result showed that in the porous probe a stress of 970 MPa induced the yield stress of 961.67 MPa. The color map of this FEM simulation is displayed below in Figure 15 only to confirm the yielded result.

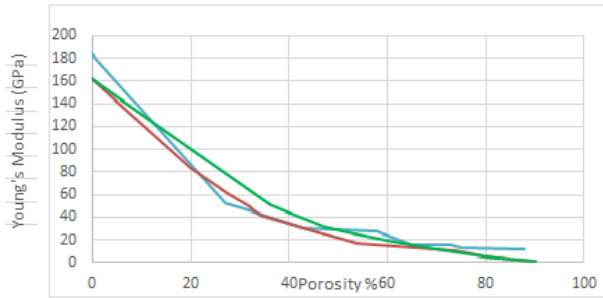


Figure 14. Different Studies on the Effect of Porosity on the Young's Modulus of Porous Silicon. The three curves are extracted from three different studies (In green [70], in blue [69], and in red [71]).

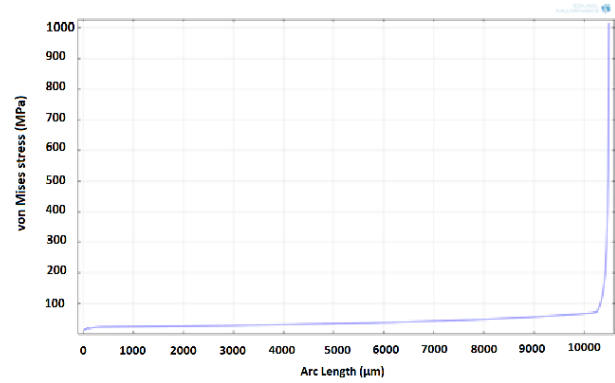


Figure 16. Von Mises stress induced upon applying an axial force along the negative x-axis versus the electrode length (non-porous).

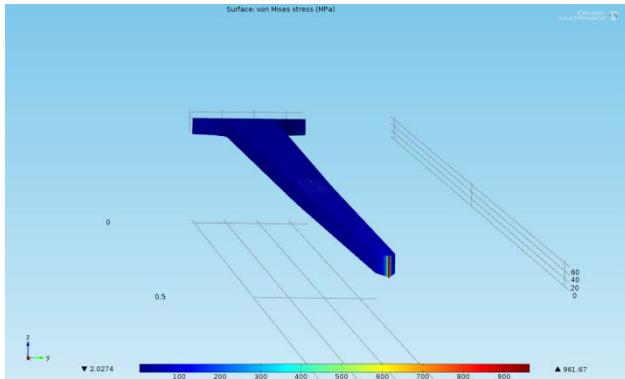


Figure 15. 3D plot of the surface stress on the electrode due to -ve x-axis axial stress at E= 185 (Porous).

That being said, the new young's modulus at our porosity (0.16%) is 184.2 GPa and the yield stress is 969.47 MPa. According to the new E, the new critical stress and force are to be calculated. The critical stress for the porous electrode was found to be equal to 8.5 MPa, and the critical force equal to 4.26 mN.

3) Results of the Application of a Compression Force Along X-axis During Penetration (Case 2)

This section demonstrates the result of the application of a single axial force that occurs directly after penetration. For the non-porous electrode, an axial stress of 1055 MPa that is equivalent to a force of 527.5 mN along the negative x-axis induced stress of around 1GPa at a length of around 10.5 mm, which corresponds to the tip of the electrode. This is depicted in Figure 16. The concentration of the induced stresses is illustrated in Figure 17.

As for the porous electrode, a force of 522.5 mN induced a similar response at a similar location as shown in Figure 19 and illustrated in Figure 18. It is worth noting that the high stress is concentrated at the tip of the electrode that is in direct contact with the brain. This contact induces the most significant stress that may cause the failure of the probe.

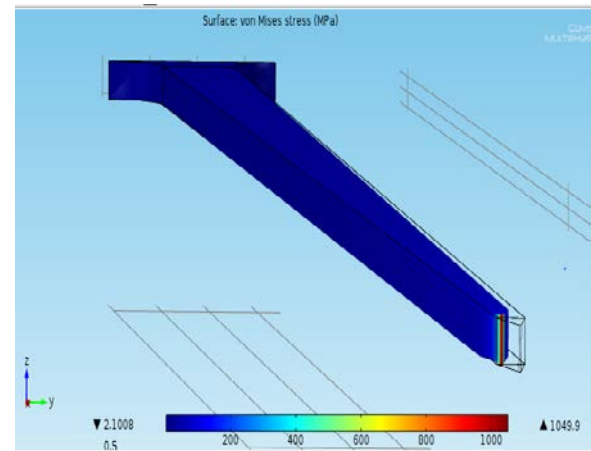


Figure 17. 3D plot of the surface stress on the electrode due to -ve x-axis axial stress (non-porous).

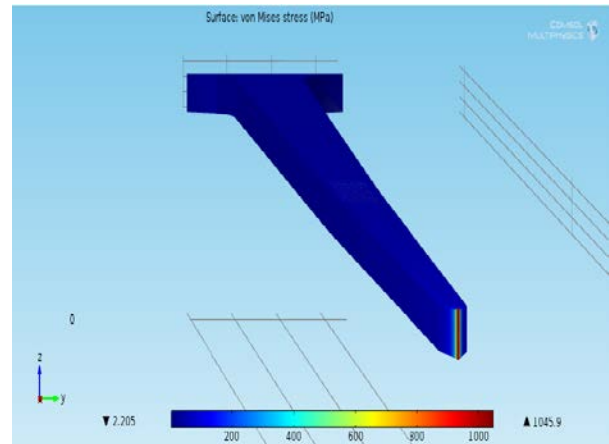


Figure 18. 3D plot of the surface stress on the electrode due to -ve x-axis axial stress (Porous).

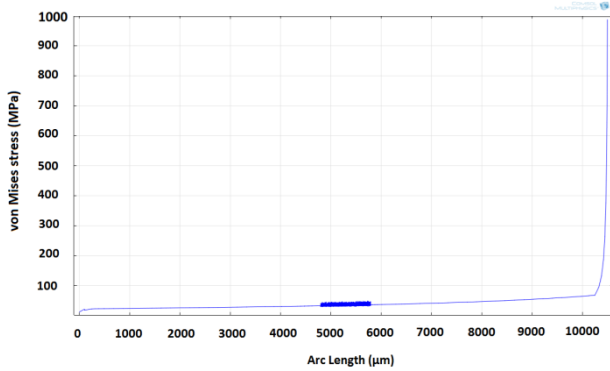


Figure 19. Von Mises stress induced upon applying an axial force along the negative x-axis versus the electrode length (porous).

4) Results of the Application of the Force Induced Due to Slipping Upon Insertion (Case 1)

This section covers the application of two axial forces (along negative x and y axes), which are imposed during the penetration phase. For the non-porous electrode, a force of 378 mN (x: 375, y: 47.5) induced a stress of ~ 1 GPa at two locations in the electrode; at a distance of ~ 5800 μm corresponding to the middle region (the blue curve in Figure 20), and at a distance of ~ 10.5 mm corresponding to the tip of the electrode (the green curve in Figure 20). The resulting surface stresses are demonstrated in Figure 21.

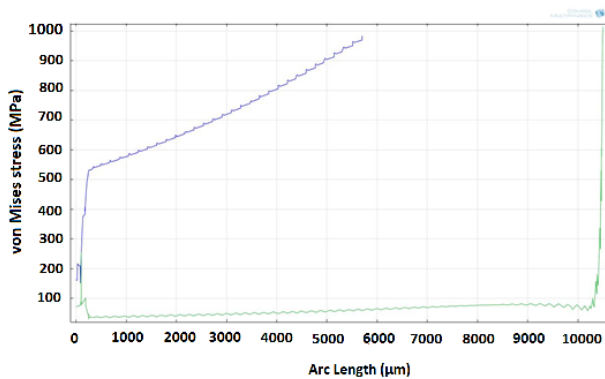


Figure 20. Von Mises stress induced upon applying an axial force along the negative y-axis versus the electrode length (non-porous).

Meanwhile, in the porous electrode, a force of 378 mN (x: 375, y: 47.5) induced a stress of ~ 1 GPa at two locations in the electrode; at a distance of ~ 5800 μm corresponding to the middle porous region (the blue curve in Figure 22), and at a distance of ~ 10.5mm corresponding to the tip of the electrode (the green curve in Figure 22). The resulting surface stresses are demonstrated in Figure 23.

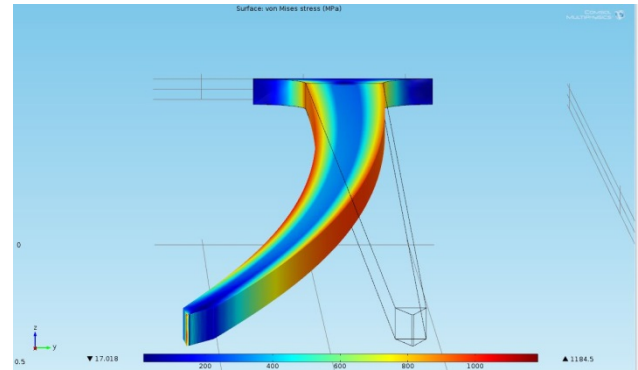


Figure 21. 3D plot of the surface stress on the electrode due a combination of axial stresses on -ve x & y axes (Non-Porous).

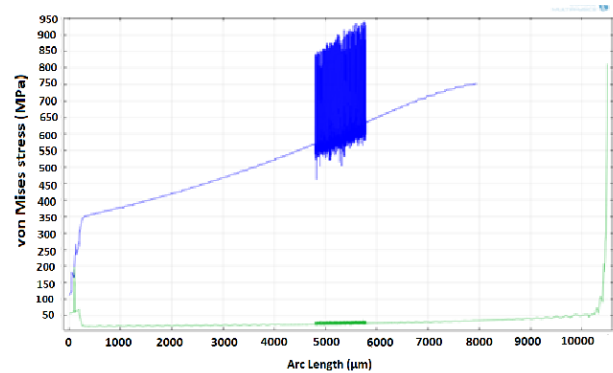


Figure 22. Von Mises stress induced upon applying an axial force along the negative y-axis versus the electrode length (porous).

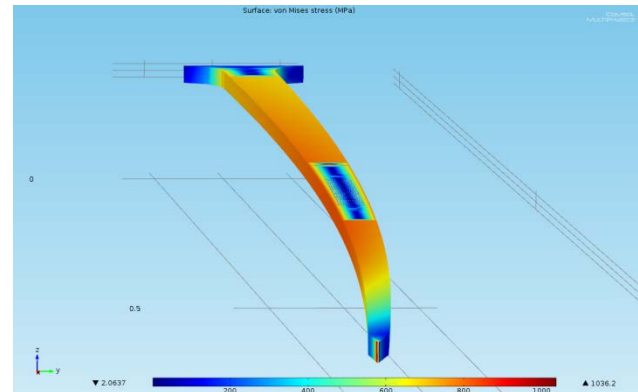


Figure 23. 3D plot of the surface stress on the electrode due a combination of axial stresses on -ve x & y axes (Porous).

5) Results of the Application of the Force Induced Upon Brain Movement After Implantation (Case 3)

Finally, this section covers the application of a vertical force that occurs after the probe implementation. For the non-porous electrode, a stress of 36.5 MPa (18.25m N) applied along the -ve z-axis induced a stress of ~ 1000 MPa (Figure 24) at a length of around 400 μm, which

corresponds to the fixed bottom region of the electrode as depicted in Figure 25.

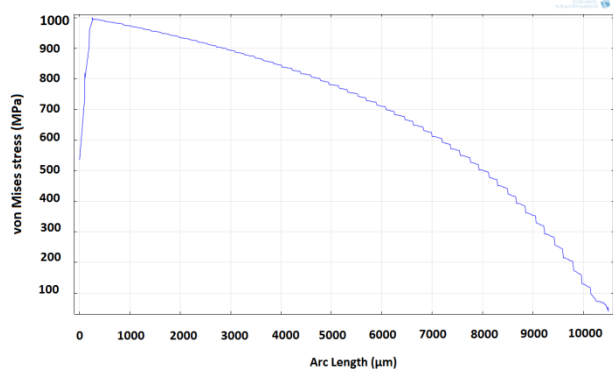


Figure 24. Von Mises stress induced upon applying a vertical force along the negative z-axis versus the electrode length (non-porous).

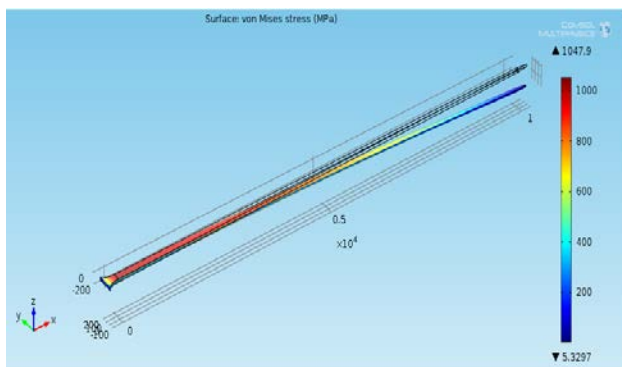


Figure 25. 3D plot of the surface stress on the electrode due to -ve z-axis vertical stress (non-porous).

On the other hand, in the porous electrode, a stress of 23 MPa (11.5 mN) applied along the -ve z-axis induced a stress of ~ 1000 MPa (Figure 26) at a length of around 750 μm, which corresponds to the weakest porous fixed bottom region of the electrode as depicted in Figure 27.

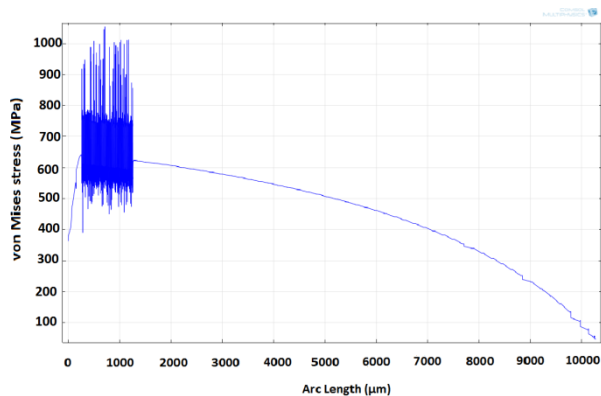


Figure 26. Von Mises stress induced upon applying a vertical force along the negative z-axis versus the electrode length (porous).

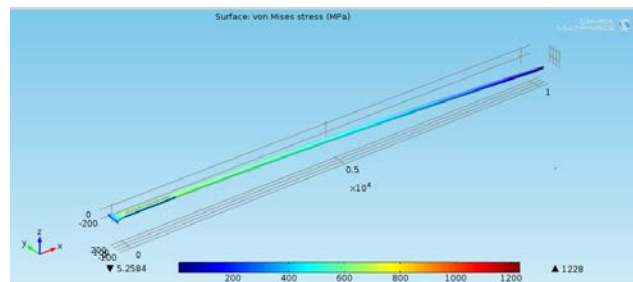


Figure 27. 3D plot of the surface stress on the electrode due to -ve z-axis vertical stress (Porous).

6) Discussion

After the mechanical behavior of the electrodes was analyzed using two different approaches, a FEM and an analytical approach, we were able to estimate the difference between the FEM model simulation and the analytical solution by a comparison of both results (Table III). This comparison showed that the similarity between the two approaches was equal to 96.76%. The minimal difference is possibly due to that FEM is a physical model and the equations cannot fully represent the model.

TABLE III. COMPARISON BETWEEN RESULTS OF POROUS AND NON-POROUS PROBES

Load along -ve x (mN)	σ_x (MPa) Non-porous	Load along -ve x (mN)	σ_x (MPa) Porous
527.5	1055	485	961
2.42	4.94 < $\sigma_{cr=8.8}$	2.42	4.94 < $\sigma'_{cr=8.5}$

On the other hand, regarding the FEM strategy performed on the three different cases, due to the comparison of the forces that induced the maximum yield stress in the three different cases for the non-porous probe (Case 1: 378 mN (x: 375, y: 47.5); Case 2: 527.5 mN; Case 3: 18.25 mN) and the ones for the porous probe (Case 1: 376.8 mN (x: 375, y: 37.5); Case 2: 522.5 mN; Case 3: 11.5 mN), one can notice the mechanical weakening of the porous silicon probe. This is true due to the fact that the values of the forces that induced the maximum yield stress in the porous probe are less than those in the non-porous probe. The weakening was 0.3 %, 0.1%, 37% in case 1, 2 and 3, respectively.

Nonetheless, this weakening will not risk the mechanical integrity of the neural probe used in brain applications. The reason is that the force that induced the maximum yield stress of the porous probe (522.5mN along the x-axis) is still much higher than the minimum force that the probe must withstand during the penetration of the brain tissue (2.42 ± 0.77 mN along the x-axis [66]).

VII. CONCLUSION

We have presented the novel idea of the mechanical simulation of a porous neural electrode. Even though the introduction of the pores relatively weakened the neural electrode, the electrode was found still capable of surviving the brain environment. Nevertheless, certain limitations were present especially related to the finite element model. The full arrays of pores could not be simulated due to computational complexity and they were restricted to the weakest areas. Moreover, different radii of pores and volume porosity percentages should be tested. The porous electrode is superior to the non-porous electrode due to the improved biocompatibility and bioactivity it offers. Furthermore, the presence of the pores gives an additional advantage where they can behave as scaffolds for entrapping neural growth factors that encourage the re-growth of neurons. This alteration to the electrode's design is able to advance the healthcare services provided to neural diseases' patients all around the world.

REFERENCES

- [1] S. B. R. Fayad, B. AbdulHay, H. Hajj-Hassan, H. Khachfe, M. Hajj-Hassan, "Modelling and Simulation of Mechanical Behaviour of an Ultra-Long Porous Silicon Neural Microelectrode," in Proc. of The Third International Conference on Global Health Challenges, Rome, Italy, pp. 50-54, 2014.
- [2] B. He, *Neural Engineering*: Springer London, Limited, 2013.
- [3] M. A. L. Nicolelis, "Brain-machine interfaces to restore motor function and probe neural circuits," *Nature Reviews Neuroscience*, vol. 4, pp. 417-422, 2003.
- [4] A. B. Schwartz, "Cortical neural prosthetics," *Annual Review of Neuroscience*, vol. 27, pp. 487-507, 2004.
- [5] K. C. Cheung, "Implantable microscale neural interfaces," *Biomed Microdevices*, vol. 9, pp. 923-938, 2007.
- [6] K. D. Wise, A.M. Sodagar, Y. Yao, M. N. Gulari, G. E. Perlin, and K. Najafi, "Microelectrodes, microelectronics, and implantable neural microsystems," *Proceedings of the IEEE*, vol. 96, pp. 1184-1202, 2008.
- [7] R. Jung, *Biohybrid Systems: Nerves, Interfaces and Machines*: Wiley, 2012.
- [8] S. F. Cogan, "Neural stimulation and recording electrodes," *Annual Review of Biomedical Engineering*, vol. 10, pp. 275-309, 2008.
- [9] T. Yoshimine, "Brain-machine interface (BMI) - application to neurological disorders," *Rinsho Shinkeigaku*, vol. 53, pp. 962-965, 2013.
- [10] P. Ponce, A. Molina, D. C. Balderas, and D. Grammatikou, *Brain Computer Interfaces for Cerebral Palsy*, 2014.
- [11] V. C. M. Hajj-Hassan, and S. Musallam, "NeuroMEMS: Neural probe microtechnologies," *Sensors*, vol. 6704-6726, pp. 6704-6726, 2008.
- [12] T. Kozai, N. Langhals, P. R. Patel, X. Deng, H. Zhang, K. L. Smith, *et al.*, "Ultrascale implantable composite microelectrodes with bioactive surfaces for chronic neural interfaces," *Nature Materials*, vol. 11, pp. 1065-1073, 2012.
- [13] F. Strumwasser, "Long-term recording from single neurons in brain of unrestrained mammals," *Science*, vol. 127, pp. 469-470, 1958.
- [14] J. C. M. Jeon, Y. K. Kim, D. Jung, E-S. Yoon, S. Shin, and I-J. Cho, "Partially flexible MEMS neural probe composed of polyimide and sucrose gel for reducing brain damage during and after implantation," *Journal of Micromechanics and Microengineering*, vol. 24, 2014.
- [15] B. Ghane-Motlagh and M. Sawan, "Design and implementation challenges of microelectrode arrays: A review " *Materials Sciences and Applications*, vol. 4, pp. 483-495 2013.
- [16] T. G. H. Yuen and W. F. Agnew, "Histological evaluation of polyesterimide-insulated gold wires in brain," *Biomaterials*, vol. 16, pp. 951-956, 1995.
- [17] J. C. Williams, R. L. Rennaker, and D. R. Kipke, "Stability of chronic multichannel neural recordings: Implications for a long-term neural interface," *Neurocomputing*, vol. 26-27, pp. 1069-1076, 1999.
- [18] D. B. M. L. Xindong, R. R. Carter, L.A. Bullara, T. G. H. Yuen, and W. F. Agnew, "Stability of the interface between neural tissue and chronically implanted intracortical microelectrodes," *IEEE Transactions on Neural Systems and Rehabilitation Engineering*, vol. 7, pp. 315-326, 1999.
- [19] D. D. M. A. L. Nicolelis, J. M. Carmena, R. Crist, G. Lehew, J. D. Kralik, and S. P. Wise, "Chronic, multisite, multielectrode recordings in macaque monkeys," *Proceedings of the National Academy of Sciences of the United States of America*, vol. 100, pp. 11041-11046, 2003.
- [20] P. F. G. Bora Kim, and M. R. Abidian, "Electrode-neural tissue interactions: Immune responses, current technologies, and future directions," in *Biomaterials Surface Science*, J. F. M. A. Taubert, and J. C. Rodriguez-Cabello, Ed., ed: Wiley-VCH, 2013.
- [21] D. A. Robinson, "The electrical properties of metal microelectrodes," *Proceedings of the IEEE*, vol. 56, pp. 1065-1071, 1968.
- [22] J. Skrzypek and E. Keller, "Manufacture of metal microelectrodes with the scanning electron microscope," *IEEE Transactions on Biomedical Engineering*, vol. 22, pp. 435-437, 1975.
- [23] C. A. Terzuolo and T. Araki, "An analysis of intra-versus extracellular potential changes associated with activity of single spinal motoneurons," *Annals of the New York Academy of Sciences*, vol. 94, pp. 547-558, 1961.
- [24] M. T. V. Tsytsarev, F. Schottler, S. Tanaka, and M. Hara, "A new planar multielectrode array: recording from a rat auditory cortex," *Journal of Neural Engineering*, vol. 3, pp. 293-298, 2006.
- [25] I. F. H. Scherberger, S. Musallam , D. J. Dubowitz, K. A. Bernheim, B. Pesaran, B. D. Corneil, B. Gilliken , and R. A. Andersen "Magnetic resonance image-guided implantation of chronic recording electrodes in the macaque intraparietal sulcus," *Journal of Neuroscience Methods*, vol. 130, pp. 1-8, 2003.
- [26] S. Musallam, M. J. Bak, P. R. Troyk, and R. A. Andersen, "A floating metal microelectrode array for chronic implantation," *Journal of Neuroscience Methods*, vol. 160, pp. 122-127, 2007.

- [27] Z. Yang, *Neural computation, neural devices, and neural prosthesis*: Springer, 2014.
- [28] D. Zhou and E. Greenbaum, *Implantable neural prostheses 2: Techniques and engineering approaches*: Springer, 2010.
- [29] R. Brette and A. Destexhe, *Handbook of neural activity measurement*: Cambridge University Press, 2012.
- [30] K. D. Wise, J. B. Angell, and A. Starr, "An integrated-circuit approach to extracellular microelectrodes," *IEEE Transactions on Biomedical Engineering*, vol. 17, pp. 238-247, 1970.
- [31] K. D. Wise and J. B. Angell, "A low-capacitance multielectrode probe for use in extracellular neurophysiology," *IEEE Transactions on Biomedical Engineering*, vol. 22, pp. 212-219, 1975.
- [32] J. K. S. Kisban, P. Janssen, R. V. Metzen, S. Herwik, U. Bartsch, T. Stieglitz, O. Paul, and P. Ruther, "A novel assembly method for silicon-based neural devices," in *World congress on medical physics and biomedical engineering*. vol. 25, O. D. a. W. C. Schlegel, Ed., ed: Springer, 2009, pp. 107-110.
- [33] E. M. M. R. A. Normann, P. J. Rousche, and D. J. Warren, "A neural interface for a cortical vision prosthesis," *Vision Research*, vol. 39, pp. 2577-2587, 1999.
- [34] P. K. C. K. E. Jones, and R. A. Normann, "A glass silicon composite intracortical electrode array," *Ann Biomed Eng*, vol. 20, 1992.
- [35] R. J. V. D. R. Kipke, J. C. Williams, and J. F. Hetke, "Silicon-substrate intracortical microelectrode arrays for long-term recording of neuronal spike activity in cerebral cortex," *IEEE Transactions on Neural Systems and Rehabilitation Engineering*, vol. 11, pp. 151-154, 2003.
- [36] K. Najafi, "Solid-state microsensors for cortical nerve recordings," *IEEE Engineering in Medicine and Biology Magazine*, vol. 13, pp. 375-387, 1994.
- [37] K. Najafi, "Micromachined systems for neurophysiological applications," in *Handbook of microlithography, micromachining, and microfabrication: Micromachining and microfabrication*, P. Rai-Choudhury, Ed., ed: SPIE Optical Engineering Press, 1997.
- [38] J. Wolpaw and E. W. Wolpaw, "Acquiring brain signals from within the brain," in *Brain-computer interfaces: Principles and practice*, ed: Oxford University Press, 2012, pp. 81-103.
- [39] D. S. P. P. J. Rousche, D. P. Pivín, J. C. Williams, R. J. Vetter, and D. R. Kipke "Flexible polyimide-based intracortical electrode arrays with bioactive capability," *IEEE Transactions on Biomedical Engineering*, vol. 48, pp. 361-371, 2001.
- [40] A. B. S. Metz, D. Bertrand, and P. Renaud, "Flexible polyimide probes with microelectrodes and embedded microfluidic channels for simultaneous drug delivery and multi-channel monitoring of bioelectric activity," *Biosensors and Bioelectronics*, vol. 19, pp. 1309-1318, 2004.
- [41] T. Stieglitz and M. Gross "Flexible BIOMEMS with electrode arrangements on front and back side as key component in neural prostheses and biohybrid systems," *Sensors and Actuators B: Chemical*, vol. 83, pp. 8-14, 2002.
- [42] T. Stieglitz, "Flexible biomedical microdevices with double-sided electrode arrangements for neural applications," *Sensors and Actuators A: Physical*, vol. 90, pp. 203-211, 2001.
- [43] H. B. T. Stieglitz, M. Schuettler, and J. Meyer, "Micromachined, polyimide-based devices for flexible neural interfaces," *Biomedical Microdevices*, vol. 2, pp. 283-294, 2000.
- [44] T. C. O. B. L. Seala, and A. Panitch, "Polymeric biomaterials for tissue and organ regeneration," *Materials Science and Engineering: R: Reports*, vol. 34, pp. 147-230, 2001.
- [45] D. C. F. J. Rodríguez, M. Schüttler, A. Valero, E. Valderrama, T. Stieglitz, and X. Navarro, "Polyimide cuff electrodes for peripheral nerve stimulation," *Journal of Neuroscience Methods*, vol. 98, pp. 105-118, 2000.
- [46] R. R. Richardson, J. A. Miller, and W. M. Reichert "Polyimides as biomaterials: preliminary biocompatibility testing," *Biomaterials*, vol. 14, pp. 627-635, 1993.
- [47] K. E. J. P. K. Campbell, R. J. Huber, K. W. Horch, and R. A. Normann, "A silicon-based, three-dimensional neural interface: manufacturing processes for an intracortical electrode array," *IEEE Transactions on Biomedical Engineering*, vol. 38, pp. 758-768, 1991.
- [48] W. L. C. Xu, and C. Liu, "Design and fabrication of a high-density metal microelectrode array for neural recording," *Sensors and Actuators A: Physical*, vol. 96, pp. 78-85, 2002.
- [49] E. F. Cristina Marin, "Biocompatibility of intracortical microelectrodes: current status and future prospects," *Frontiers in Neuroengineering*, vol. 3, 2010.
- [50] B. G. E. Fernández, P. A. House, I. Aranda, C. Botella, J. Albisua, C. Soto-Sánchez, A. Alfaro, and R. A. Normann, "Acute human brain responses to intracortical microelectrode arrays: challenges and future prospects," *Frontiers in Neuroengineering* vol. 7, pp. 1-6, 2014.
- [51] P. A. T. V. S. Polikov, and W. M. Reichert, "Response of brain tissue to chronically implanted neural electrodes," *Journal of Neuroscience Methods*, vol. 148, pp. 1-18, 2005.
- [52] W. S. J. N. Turner, D. H. Szarowski, M. Andersen, S. Martins, M. Isaacson, and H. Craighead, "Cerebral astrocyte response to micromachined silicon implants," *Experimental Neurology*, vol. 156, pp. 33-49, 1999.
- [53] S. S. Stensaas and L. J. Stensaas, "The reaction of the cerebral cortex to chronically implanted plastic needles," *Acta neuropathologica*, vol. 35, pp. 187-203, 1976.
- [54] J. P. Seymour and D. R. Kipke, "Neural probe design for reduced tissue encapsulation in CNS," *Biomaterials*, vol. 28, pp. 3594-3607, 2007.
- [55] H. D. R. G. C. McConnell, A. I. Levey, C. A. Gutekunst, R. E. Gross, and R. V. Bellamkonda, "Implanted neural electrodes cause chronic, local inflammation that is correlated with local neurodegeneration," *Journal of Neural Engineering*, vol. 6, p. 056003, 2009.
- [56] M. D. A. D. H. Szarowski, S. Retterer, A. J. Spence, M. Isaacson, H. G. Craighead, J. N. Turner, and W. Shain "Brain responses to micro-machined silicon devices," *Brain Research*, vol. 983, pp. 23-35, 2003.
- [57] E. J. K. N. K. Wood, and R. J. Oglesby, "The significance of implant shape in experimental testing of biological materials: Disc vs. Rod," *Journal of Biomedical Materials Research*, vol. 4, pp. 1-12, 1970.

- [58] S. R. Taylor and D. F. Gibbons, "Effect of surface texture on the soft tissue response to polymer implants," *Journal of Biomedical Materials Research*, vol. 17, pp. 205-227, 1983.
- [59] A. Rosengren, L.M. Bjursten, N. Danielsen, H. Persson, and M. Kober, "Tissue reactions to polyethylene implants with different surface topography," *Journal of Materials Science: Materials in Medicine*, vol. 10, pp. 75-82, 1999.
- [60] L. W. Agneta Rosengren, Nils Danielsen, Thomas Laurell, and Lars Magnus Bjursten, "Tissue Reactions Evoked by Porous and Plane Surfaces Made Out of Silicon and Titanium," *IEEE Transactions on Biomedical Engineering*, vol. 49, 2002.
- [61] S. H. K. A. Moxon, A. Aslani, N. M. Kalkhoran, and P. I. Lelkes, "Bioactive properties of nanostructured porous silicon for enhancing electrode to neuron interfaces," *Journal of Biomaterials Science, Polymer Edition*, vol. 18, pp. 1263-1281, 2007.
- [62] M. Hajj-Hassan M, H. Wang, V. Chodavarapu, and J.E. Henderson, "Response of murine bone marrow-derived mesenchymal stromal cells to dry-etched porous silicon scaffolds," *Journal of Biomedical Materials Research Part A*, 2011.
- [63] C. J. Wilson and P. A. Beck, "Fracture Testing of Bulk Silicon Microcantilever Beams Subjected to a Side Load," *Journal of Microelectromechanical Systems*, vol. 5, pp. 142-150, 1996.
- [64] A. Blake, *Handbook of Mechanics, Materials, and Structures*: Wiley, 1985.
- [65] J. A. Collins, H. R. Busby, and G. H. Staab, *Mechanical Design of Machine Elements and Machines*: Wiley, 2010.
- [66] M. Hajj-Hassan, and S. Musallam, "Reinforced silicon neural microelectrode array fabricated using a commercial MEMS process," *Journal of Micro/Nanolithography, MEMS, and MOEMS*, vol. 8, p. 033011, 2009.
- [67] J. Gere and B. Goodno, *Mechanics of Materials*: Cengage Learning, 2008.
- [68] M. Hajj-Hassan, and S. Musallam, "Reinforced silicon neural microelectrode array fabricated using a commercial MEMS process," *Journal of Micro/Nanolithography, MEMS, and MOEMS*, vol. 8, 2009.
- [69] Y. Al-Douri, N. M. Ahmed, N. Bouarissa, and A. Bouhemadou, "Investigated optical and elastic properties of Porous silicon: Theoretical study," *Materials and Design*, vol. 32, pp. 4088-4093, 2011.
- [70] D. Bellet, P. Lamagnere, A. Vincent, and Y. Bréchet, "Nanoindentation investigation of the Young's modulus of porous silicon," *Journal of Applied Physics*, vol. 80, 1996.
- [71] "Nanocrystalline Porous Silicon," in *Crystalline Silicon - Properties and Uses*, S. Basu, Ed., ed: InTech, 2011.